


# Spiking-bursting alternating chaos mediated by a locally active memristor

Yuxia Li(李玉霞), Xintong Yue(岳新同), Hui Chang(常辉), Baoxing Han(韩宝兴), and Yan Zhang(张燕)
**Citation:**Chin. Phys. B, 2026, 35 (**3**): 030504. DOI: 10.1088/1674-1056/ae44f9
http://cpb.iphy.ac.cn; http://iopscience.iop.org/cpb

**What follows is a list of articles you may be interested in**

---

## Memristors-coupled neuron models with multiple firing patterns and homogeneous and heterogeneous multistability

Xuan Wang(王暄), Santo Banerjee, Yinghong Cao(曹颖鸿), and Jun Mou(牟俊)
Chin. Phys. B, 2024, 33 (**10**): 100501. DOI: 10.1088/1674-1056/ad6256

## Dynamics analysis and cryptographic implementation of a fractional-order memristive cellular neural network model

Xinwei Zhou(周新卫), Donghua Jiang(蒋东华), Jean De Dieu Nkapkop, Musheer Ahmad, Jules Tagne Fossi, Nestor Tsafack, and Jianhua Wu(吴建华)
Chin. Phys. B, 2024, 33 (**4**): 040506. DOI: 10.1088/1674-1056/ad03dd

## Dynamical analysis, geometric control and digital hardware implementation of a complex-valued laser system with a locally active memristor

Yi-Qun Li(李逸群), Jian Liu(刘坚), Chun-Biao Li(李春彪), Zhi-Feng Hao(郝志峰), and Xiao-Tong Zhang(张晓彤)
Chin. Phys. B, 2023, 32 (**8**): 080503. DOI: 10.1088/1674-1056/acd68b

## Power-law statistics of synchronous transition in inhibitory neuronal networks

Lei Tao(陶蕾) and Sheng-Jun Wang(王圣军)
Chin. Phys. B, 2022, 31 (**8**): 080505. DOI: 10.1088/1674-1056/ac5c31

## Negative self-feedback induced enhancement and transition of spiking activity for class-3 excitability

Li Li(黎丽), Zhiguo Zhao(赵志国), and Huaguang Gu(古华光)
Chin. Phys. B, 2022, 31 (**7**): 070506. DOI: 10.1088/1674-1056/ac4a63

---

# Spiking-bursting alternating chaos mediated by a locally active memristor

Yuxia Li(李玉霞)[1], Xintong Yue(岳新同)[1], Hui Chang(常辉)[1,†], Baoxing Han(韩宝兴)[1], and Yan Zhang(张燕)[2]

[1] *College of Electrical and Automation Engineering, Shandong University of Science and Technology, Qingdao* 266590, *China*
[2] *College of Safety and Environmental Engineering, Shandong University of Science and Technology, Qingdao* 266590, *China*

(Received 5 December 2025; revised manuscript received 10 February 2026; accepted manuscript online 12 February 2026)

Local active memristors demonstrate complex nonlinear dynamic characteristics under specific voltage stimuli, making them well-suited for emulating biological synapse behavior. This paper presents a novel local active memristor with coexisting hysteresis loops, whose non-volatility and local activity are experimentally verified. Based on this memristor, a spiking-bursting chaotic system is constructed, which can reproduce neuronal firing patterns such as periodic spiking, bursting and spiking-bursting alternating discharge. In addition, it reveals the generation mechanism of the spiking-bursting alternating chaos driven by the locally active memristor. Finally, the chaotic system is physically implemented on a field-programmable gate array (FPGA). The experimental results show excellent agreement with numerical simulations, confirming the system's feasibility and highlighting its potential for engineering applications.

**Keywords:** locally active memristor, spiking, chaotic bursting, FPGA

**PACS:** 05.45.–a, 95.10.Fh, 84.30.–r

**DOI:** 10.1088/1674-1056/ae44f9 **CSTR:** 32038.14.CPB.ae44f9

## 1. Introduction

Originating from the construction and analysis of climate models,[1–4] chaos theory has achieved breakthroughs in domains such as time series prediction,[5] data encryption,[6,7] and optimization algorithms.[8] Due to their inherent nonlinearity, memristors offer a natural advantage in constructing chaotic systems. In recent years, a series of memristive chaotic circuits and systems have been developed, exhibiting complex dynamical behavior including transient chaos,[9] sustained chaos,[10] coexisting attractors,[11,12] hidden attractors,[13,14] extreme multistability[15–17] and intermittent chaos.[18–22] However, a survey of the literature,[23,24] indicates that the analysis of biomimetic characteristics in memristive systems remains relatively scarce, and thus deserves further investigation.

Local activity, as the origin of complexity, provides a theoretical foundation for the discovery of locally active memristors.[25] The presence of locally active domains in memristors can elicit rich biomimetic dynamics in memristive chaotic systems.[26–28] For instance, a coupled neuron model incorporating a locally active discrete memristor has been exhibited to induce hyperchaotic attractors under enhancing electromagnetic radiation intensity.[29] A locally active tristable memristor was introduced into chaotic circuits, demonstrating its capability to generate complex dynamics from locally active regions through the progressive integration of circuit components.[30] In addition, a chaotic circuit based on a local active memristor has been constructed, exhibiting neuromorphic dynamics.[31] Another widely explored research direction involves using memristors to emulate synaptic functions, either for coupling neurons or for constructing neural networks. Within these systems, a variety of novel and interesting phenomena are reported. For instance, in a memristor-coupled discrete heterogeneous neuron network, multiple coexisting firing patterns have been observed. In addition, Gaussian white noise has been found to both induce transitions in neuronal firing patterns and promote phase synchronization between the two heterogeneous neurons.[32] Under the influence of an ideal memristor serving as an external electromagnetic stimulation and a locally active memristor serving as a synapse, the Hindmarsh–Rose neuron model exhibits multiple burst firing patterns.[33] Moreover, hidden attractors have been identified in a novel 4D fractional-order memristive cellular neural network model, which demonstrates promising performance in data encryption.[34] However, most existing studies on biomimetic characteristics rely on mathematical models fitted to biological neuronal discharge data, rather than on the memristor system itself. In contrast, the locally active memristive system proposed in this paper intrinsically exhibits distinctive neuronal firing behavior, providing an approach to neuromorphic modeling.

The dynamic behavior of biological neurons underpins information transmission and neural coding. Simulating these complex neuronal dynamics is therefore of great scientific importance. It also remains a challenging research topic. At present, significant progress has been made in simulating neu-

[†]Corresponding author. E-mail: changhui2000_mic@sdust.edu.cn

© 2026 Chinese Physical Society and IOP Publishing Ltd. All rights, including for text and data mining, AI training, and similar technologies, are reserved.

ronal firing behavior. For example, one study observed a dynamical evolution from intermittent bursting to chaotic bursting, then to periodic bursting, and finally to synchronization in a feedback-based chaotic oscillator.[35] Another study found that memristive chaotic circuits can exhibit both chaotic and periodic bursting depending on initial conditions.[36] External stimuli have also been shown to induce various periodic spiking and chaotic bursting patterns in memristive Hodgkin–Huxley (MHH) models.[37] Despite these advances, the specific phenomenon of the alternating spiking-bursting discharge has been rarely explored. In light of this, this paper proposes a novel memristive chaotic system that generates alternating spiking-bursting discharges and systematically explores its complex dynamics. This deepens our understanding of spiking-bursting discharge.

Furthermore, memristive systems are highly practical in many engineering disciplines.[38,39] Implementing these systems on hardware platforms like FPGAs is crucial for real-world applications since FPGAs provide a direct interface to the digital world.[40–42] In this study, the proposed memristive system is successfully implemented on an FPGA. An improved Euler algorithm is applied for numerical integration. The experimental results captured from the oscilloscope show excellent agreement with numerical simulations, verifying the system's physical realizability.

The remainder of the paper is arranged as follows. Section 2 presents the design and theoretical analysis of a novel spiking-bursting chaotic system based on a locally active memristor. Section 3 investigates the dynamic behavior of the chaotic system through numerical simulations. Section 4 details the FPGA implementation of the proposed memristive chaotic system. Finally, Section 5 provides concluding remarks.

## 2. Memristor-based chaotic system

### 2.1. Memristor emulator

In this section, a novel memristor emulator is designed, as illustrated in Fig. 1.

The circuit comprises an inverting amplifier, a multiplier and multiple resistors. A sinusoidal AC voltage signal, $v_{\rm in}$, is applied as an input, while the output is measured as the current $i$.

To explore the dynamic characteristics of the system, the dynamics are derived based on Kirchhoff's laws

$$\begin{cases} \dfrac{{\rm d}X}{{\rm d}t} = -\dfrac{1}{CR_3}X^3 + \dfrac{1}{CR_2}X^2 + \dfrac{1}{CR_1}X + \dfrac{v_{\rm in}}{CR_5} - \dfrac{1}{CR_4}v_1, \\ i = \left(\dfrac{R_{04}}{R_{07}}X + \dfrac{R_{04}}{R_{03}}X^2\right)v_{\rm in}. \end{cases} \tag{1}$$

Extensive experimental measurements have yielded specific values for the physical components, including $C$, $R_1$, $R_2$, $R_3$, $R_4$, $R_5$, $R_{03}$, $R_{04}$ and $R_{07}$, as summarized in Table 1. Circuit simulations of the design shown in Fig. 1 were performed using Multisim. The memristor was stimulated by a voltage signal defined as $v_{\rm in} = v_{\rm m}\sin(2\pi ft)$. Hysteresis loops were captured under an amplitude $v_{\rm m} = 4$ V and frequency $f = 1$ Hz, $f = 5$ Hz and $f = 20$ Hz, as depicted in Fig. 2. It was observed that the area of the hysteresis loop progressively shrank as the frequency $f$ increased. Furthermore, as the frequency approached infinity, the hysteresis loop collapsed into a single-valued function, which aligns with the recognized fingerprint characteristics of memristors.[43]

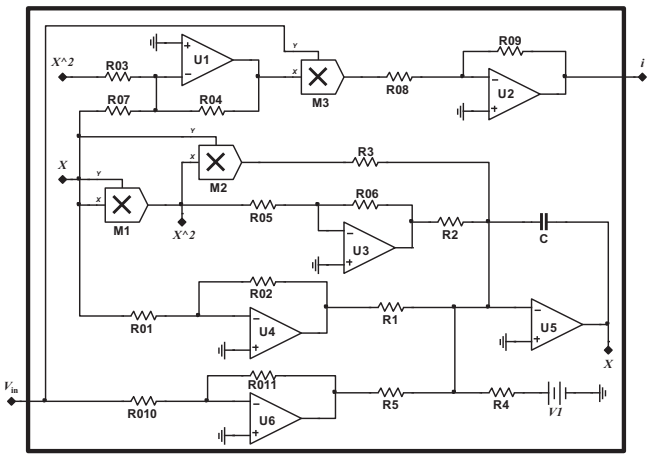



**Fig. 1.** Circuit design of the memristor emulator.

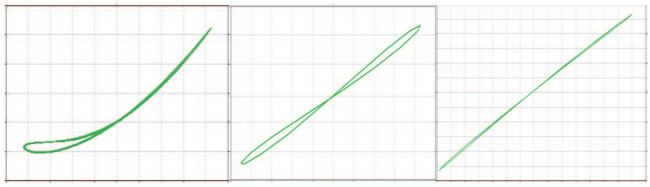


**Fig. 2.** Hysteresis loops of the memristor under the stimulus $v_{\rm in} = v_{\rm m}\sin(2\pi ft)$ with frequencies (a) $f = 1$ Hz, (b) $f = 5$ Hz, (c) $f = 20$ Hz, and $v_{\rm m}$ is fixed at 4 V.

**Table 1.** Internal parameters of the memristor emulator.

| Internal parameters | Values | Units |
|---|---|---|
| $C_1$ | 100 | nF |
| $R_1$ | 10 | kΩ |
| $R_2$ | 50 | kΩ |
| $R_3$ | 33.333 | kΩ |
| $R_4$ | 100 | kΩ |
| $R_5$ | 100 | kΩ |
| $R_{03}$ | 20 | kΩ |
| $R_{04}$ | 20 | kΩ |
| $R_{07}$ | 20 | kΩ |

Experimental analysis indicates that the graph enclosed by the power-off plot (Fig. 3) and the horizontal line ${\rm d}X/{\rm d}t = 0$ is symmetrical and has an equal area under the external voltage stimulation $\frac{1}{CR_4}v_1 = 2$. The memristor has three equilibrium points: $Q_0$ (0, 0), $Q_1$ $(-1.6, 0)$, and $Q_2$ (2.1,0). The arrows denote the evolution direction of the memristor states. From this, it can be inferred that points $Q_1$ and $Q_2$ are asymptotically stable, while point $Q_0$ is unstable. The internal charge

filling and release within the memristor achieve a balance, thereby gradually approaching static equilibrium points in a power-off state.

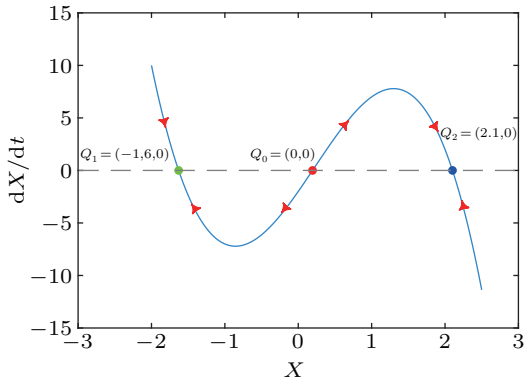



**Fig. 3.** Memristor dynamics with $\frac{1}{CR_4}v_1 = 2$.

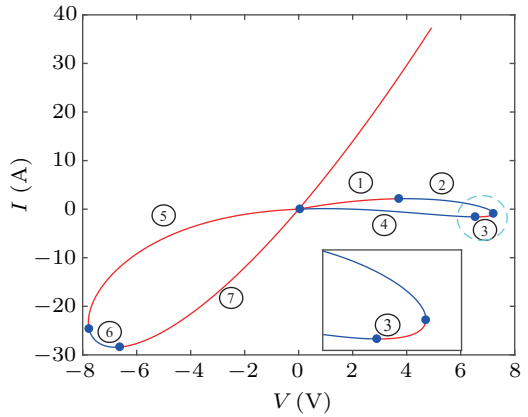



**Fig. 4.** DC $V$–$I$ plot of the memristor.

This study further investigates the memristor dynamics under DC excitation. When the system is in a steady state ($\mathrm{d}X/\mathrm{d}t = 0$) under DC voltage excitation, the relationship between the DC voltage $V$ and the internal state $X$ can be derived as follows:

$$V = 3X^3 - 2X^2 - 10X + 2 = v_{\text{in}}(X). \tag{2}$$

Substituting Eq. (2) into Eq. (1) and simplifying yields the relationship between $V$ and $I$:

$$\begin{aligned} I &= (X + X^2)(3X^3 - 2X^2 - 10X + 2) \\ &= 3X^5 + X^4 - 12X^3 - 8X^2 + 2X. \end{aligned} \tag{3}$$

The DC $V$–$I$ characteristic curve in Fig. 4, which plots the relationship between $V$ and $I$ from Eqs. (2) and (3), depicts the memristor's local activity and passivity. Local activity describes the local energy behavior of a device in response to small-signal perturbations when it is biased at a specific DC equilibrium point. This means that within the local activity region, the device can convert energy from the DC bias into energy for small AC signals, thereby amplifying disturbances or noise at specific frequencies. This mechanism serves as the origin for generating complex nonlinear dynamics such as oscillations and chaos. In the DC $V$–$I$ plot of a memristor, the segment with a negative slope ($\mathrm{d}I/\mathrm{d}V$) corresponds to its local activity region, where the memristor is more prone to exhibit complex dynamic behavior. According to Fig. 4 and the enlarged image adjacent to curve segment ③, locally active regions are marked in blue (②, ④, ⑥), and locally passive regions are marked in red (①, ③, ⑤, ⑦). Table 2 provides the particulars of the three locally active domains.

**Table 2.** Local active regions of the memristor.

| $X$ | Voltage (V) | Current (A) |
|---|---|---|
| (0.19, 1.35) | (−7.764, −6.622) | (−28.386, −24.631) |
| (−1.41, 0.85) | (3.714, 7.213) | (−0.920, 2.147) |
| (−0.58, 0.19) | (0.048, 6.542) | (−1.594, 0.011) |

## 2.2. Chaotic system construction

A chaotic circuit system was designed using the memristor mentioned above, as shown in Fig. 5. This system consists of four nonlinear components, including two capacitors, an inductor and a memristor.

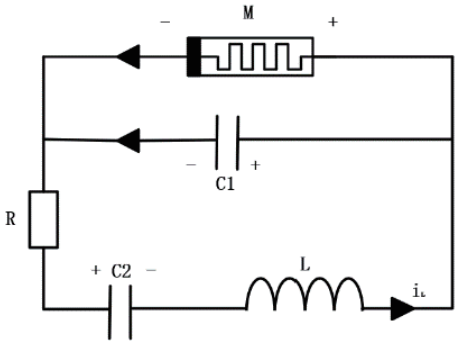



**Fig. 5.** Chaotic circuit based on the locally active memristor.

Based on the characteristics of a parallel circuit, the voltages across the memristor and capacitor C1 are equal, i.e., $v = v_{\text{C1}}$. Using the memristor parameters provided in Table 1, the dynamics of the memristive chaotic circuit are governed by the following set of equations:

$$\begin{cases} \dfrac{\mathrm{d}X}{\mathrm{d}\tau} = -3X^3 + 2X^2 + 10X + v_{\text{C1}} - 2, \\ \dfrac{\mathrm{d}i_{\text{L}}}{\mathrm{d}\tau} = -\dfrac{R}{L}i_{\text{L}} - \dfrac{1}{L}\left(v_{\text{C1}} + v_{\text{C2}}\right), \\ \dfrac{\mathrm{d}v_{\text{C1}}}{\mathrm{d}\tau} = -\dfrac{R_{04}}{C_1 R_{07}}x v_{\text{C1}} - \dfrac{R_{04}}{C_1 R_{03}}x^2 v_{\text{C1}} + \dfrac{1}{C_1}i_{\text{L}}, \\ \dfrac{\mathrm{d}v_{\text{C2}}}{\mathrm{d}\tau} = \dfrac{1}{C_2}i_{\text{L}}. \end{cases} \tag{4}$$

Here, $i_{\text{L}}$ represents the current flowing through the inductor L, and $v_{\text{C1}}$ and $v_{\text{C2}}$ represent the voltages across capacitors C1 and C2, respectively. The characteristic voltage $V_{\text{bias}}$ corresponding to the equilibrium point $Q_2$ ($X = 2.1$) of the memristor is 27.9 V. To derive the dimensionless form of Eq. (4), the $V_{\text{bias}}$ is chosen as the reference voltage, while resistor $R$

and capacitor $C_2$ in Fig. 5 are taken as the reference resistor and reference capacitor, respectively, i.e., $V_\mathrm{r} = V_\mathrm{bias} = 27.9$ V, $R_\mathrm{r} = R$, $C_\mathrm{r} = C_2$. We define

$$\begin{cases} x = XR_\mathrm{r},\ y = \frac{i_\mathrm{L}R_\mathrm{r}}{V_\mathrm{r}},\ z = \frac{v_\mathrm{C1}}{V_\mathrm{r}},\ w = \frac{v_\mathrm{C2}}{V_\mathrm{r}} = \frac{\tau}{R_\mathrm{r}C_\mathrm{r}},\ b_1 = \frac{RR_\mathrm{r}C_\mathrm{r}}{L}, \\ b_2 = \frac{R_\mathrm{r}^2C_\mathrm{r}}{L},\ c_1 = \frac{C_\mathrm{r}R_{04}}{C_1R_{07}},\ c_2 = \frac{C_\mathrm{r}R_{04}}{C_1R_{03}},\ c_3 = \frac{C_\mathrm{r}}{C_1},\ m = \frac{C_\mathrm{r}}{C_2}. \end{cases} \tag{5}$$

Substituting Eq. (5) into Eq. (4) and performing simplification and rearrangement yield the normalized dynamics

$$\begin{cases} \dfrac{\mathrm{d}x}{\mathrm{d}t} = -3x^3 + 2x^2 + 10x + z - 2, \\ \dfrac{\mathrm{d}y}{\mathrm{d}t} = -b_1 y - b_2\,(z + w)\,, \\ \dfrac{\mathrm{d}z}{\mathrm{d}t} = -c_1 xz - c_2 x^2 z + c_3 y, \\ \dfrac{\mathrm{d}w}{\mathrm{d}t} = my. \end{cases} \tag{6}$$

The system parameters, determined through iterative experimental refinement, are provided in Table 3. Using these parameters and initial conditions $(x(0), y(0), z(0), w(0)) = (0, 0, 0.1, 0)$, the four Lyapunov exponents for system (6) were calculated via the Wolf method, yielding LE1 $= 0.064$, LE2 $= -0.003$, LE3 $= -3.800$ and LE4 $= -18.571$, and the positivity of LE1 indicates the existence of chaos in the system. Furthermore, the system exhibits a spiking-bursting alternating chaotic behavior, as depicted in Fig. 6(a). This state comprises two primary discharge modes: bursting discharge, characterized by high-frequency activity analogous to rapid neuronal firing, and spiking discharge, marked by sudden intensifications that manifest as sharp oscillations or large-amplitude transitions. The corresponding phase trajectory of the spiking-bursting alternation is presented in Fig. 6(b), representing the observed and novel discharge phenomenon.

The mechanism governing the spiking-bursting alternating chaos is explored as follows. Figure 6(a) shows that this discharge pattern occurs for the memristor voltage $v_\mathrm{C1}$, the corresponding state $z$ in the interval $(-7.764, 7.213)$. This range shows a high degree of coincidence with the memristor's locally active regions displayed in Fig. 4. This correlation suggests that the memristor's local activity initiates the spiking-bursting phenomenon. Specifically, in a locally active region, the system gains energy, causing a gradual amplitude growth. Upon surpassing a critical point, the state experiences a rapid energy release, manifesting as a spike. The system then enters a locally passive region where energy decays, giving rise to a bursting cluster. This cycle of energy infusion and dissipation underpins the chaotic spike-cluster alternation. The subsequent section provides a theoretical stability analysis.

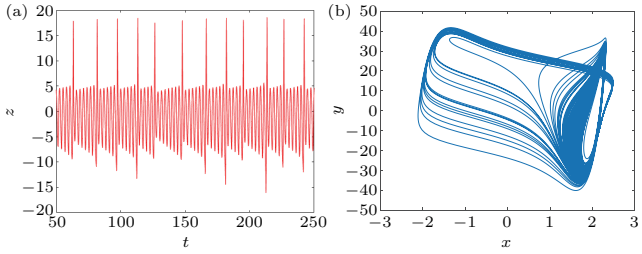



**Fig. 6.** Emergent spiking-bursting behavior at $c_3 = 1.24$. (a) Temporal evolution of the state variable $z$ and (b) phase trajectory projected onto the $z$–$w$ plane.

**Table 3.** Parameter values of the memristive chaotic system.

| Parameters | $b_1$ | $b_2$ | $c_1$ | $c_2$ | $c_3$ | $m$ |
|---|---|---|---|---|---|---|
| Value | $-1$ | 5.4 | 1 | 1 | 1.24 | 0.8 |

## 3. Dynamics analysis

### 3.1. Stability

Setting the left-hand side of Eq. (6) to zero after substituting the parameter values from Table 3 yields

$$\begin{cases} -3x^3 + 2x^2 + 10x + z - 2 = 0, \\ y - 5.4\,(z + w) = 0, \\ -xz - x^2 z + 1.24y = 0, \\ 0.8y = 0. \end{cases} \tag{7}$$

Let $E_n = (e_1, e_2, e_3, e_4)$ be an equilibrium point of the system. Then, the equilibrium Eq. (7) yields

$$\begin{aligned} E_n = \{&(e_1, e_2, e_3, e_4) \in R | e_1 e_3 (1 + e_1) = 0, \\ &e_2 = 0,\ e_3 + e_4 = 0\}. \end{aligned} \tag{8}$$

The local stability of the equilibrium point can be assessed by analyzing the associated eigenvalues. The Jacobian matrix is derived via the local linearization of the system about the equilibrium point, as follows:

$$J = \begin{bmatrix} -9x^2 + 4x + 10 & 0 & 1 & 0 \\ 0 & 1 & -5.4 & -5.4 \\ -z - 2xz & 1.24 & -x - x^2 & 0 \\ 0 & 0.8 & 0 & 0 \end{bmatrix}. \tag{9}$$

The eigenvalues and stability of the equilibrium points are summarized in Table 4. The analysis indicates that equilibrium points $E_1$, $E_2$, $E_5$ and $E_6$ are unstable saddle-foci, $E_3$ is an unstable focus and $E_4$ is a stable node-focus. The presence of these saddle-foci is critical since they can give rise to complex and unpredictable phase-space trajectories. A detailed analysis of the system's dynamic evolution follows.

### 3.2. Dynamic evolution of the system

The bifurcation diagram and Lyapunov exponents of the system with parameter $c_3$ are obtained, as illustrated in Fig. 7, with the initial conditions (0, 0, 0.1, 0) and the parameter values listed in Table 3. It can be seen from Fig. 7(a) that the system enters a chaotic state through a boundary crisis at

$c_3 = 1.04$, and this state persists until $c_3 = 1.1124$. As $c_3$ increases, the system undergoes another boundary crisis and degenerates into a periodic discharge pattern. Subsequently, when $c_3$ increases to 1.157, the system switches to chaos, persisting until $c_3 = 1.27$. When $c_3 > 1.27$, the system undergoes transitions to a distinct dynamical state, as exemplified by $c_3 = 1.3$ in Fig. 8(a). It is characterized by trajectories that are first attracted to the stable node-focus $E_4$ $(-1.6, 0, 0, 0)$ before being diverted by the influence of other equilibria. Due to the global dominant role of the unstable saddle-focus $E_6$ (2.1, 0, 0, 0), a periodic discharge emerges, which stems from the local dynamics around it. As $c_3$ continuously increases, the system undergoes another state transition at $c_3 = 1.38$, shifting from the periodic discharge mode to another, as shown in Fig. 8(b). Its characteristic is that the system is initially attracted by point $E_4$, then moves away from it. Under the strong attraction of $E_6$, the system is pulled and attracted constantly, and finally oscillates weakly around it, but cannot form a point attractor. This unconventional phenomenon primarily arises from the interplay among equilibrium points, signal amplification by locally active memristors, and the particularly strong attractive strength of equilibrium point $E_6$.

**Table 4.** The corresponding eigenvalues and stability of the equilibria.

| Equilibria | Eigenvalues | Stability |
|---|---|---|
| $E_1$ $(-1, 0, 7, -7)$ | $4.2077, -0.8472, 0.3198 \pm 2.8833\mathrm{i}$ | unstable saddle-focus |
| $E_2$ $(-1, 0, 0, 0)$ | $0, -3, 0.5 \pm 3.2787\mathrm{i}$ | unstable saddle-focus |
| $E_3$ $(0, 0, 2, -2)$ | $0.4409 \pm 3.3052\mathrm{i}, 0.0591 \pm 0.8795\mathrm{i}$ | unstable focus |
| $E_4$ $(-1.6, 0, 0, 0)$ | $-18.7783, -0.4168, -0.1024 \pm 2.2078\mathrm{i}$ | stable node-focus |
| $E_5$ $(0.2, 0, 0, 0)$ | $8.3701, -0.095, 0.8625 \pm 3.5877\mathrm{i}$ | unstable saddle-focus |
| $E_6$ $(2.1, 0, 0, 0)$ | $-33.6754, -3.5495, 0.2625 \pm 2.2226\mathrm{i}$ | unstable saddle-focus |

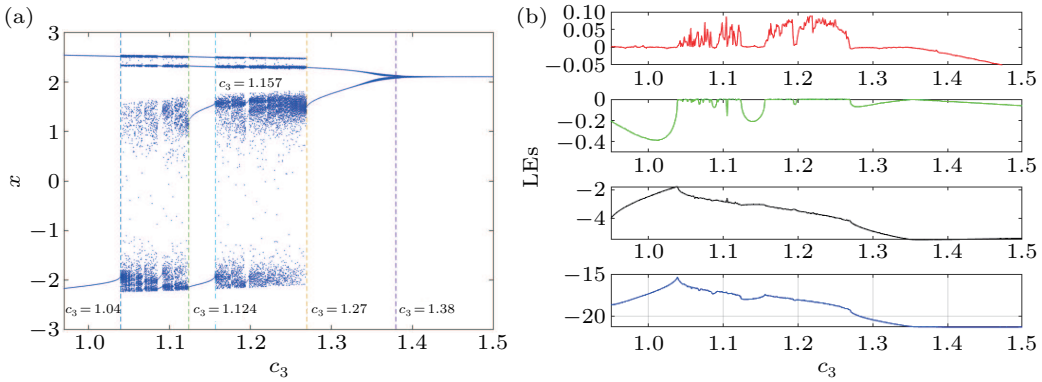



**Fig. 7.** (a) Bifurcation diagram and (b) Lyapunov exponents of the system with the parameter $c_3$ varying in the range (0.95, 1.5).

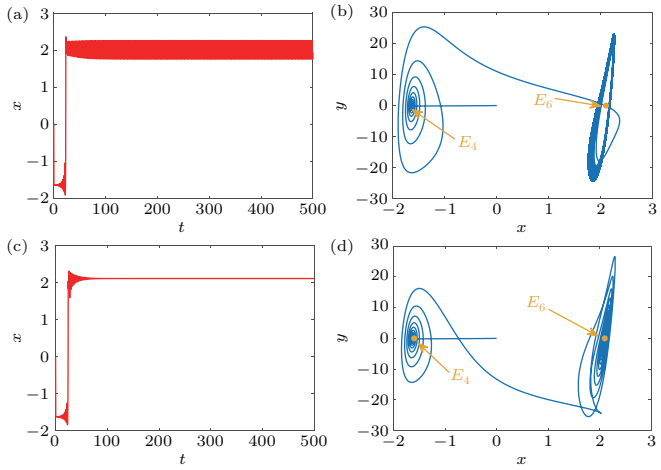



**Fig. 8.** Dynamical evolution of the system between equilibrium points. (a) Temporal evolution of the state $x$ and (b) phase trajectory on the $x$–$y$ plane with $c_3 = 1.3$; (c) temporal evolution of the state $x$ and (d) phase trajectory on the $x$–$y$ plane with $c_3 = 1.38$.

The system exhibits a chaotic bursting phenomenon at parameter $c_3 = 1.05$, as shown in Figs. 9(a) and 9(b). Periodic spiking occurs at parameter $c_3 = 1$, as shown in Figs. 9(c) and 9(d). This demonstrates that the memristive chaotic system has discharge behavior similar to that of the nervous system.

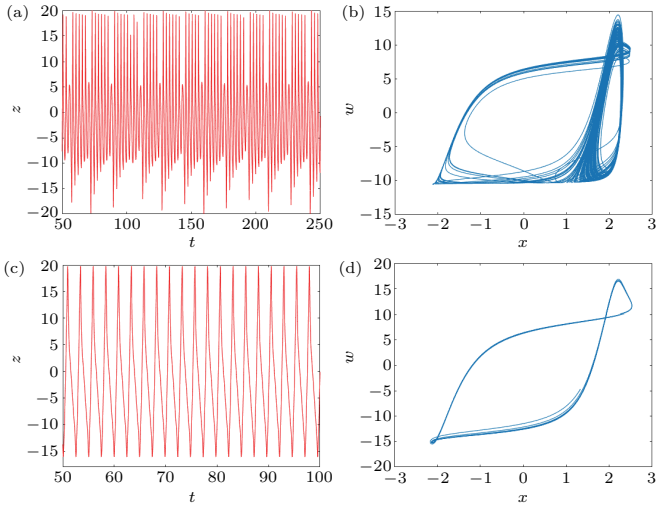



**Fig. 9.** Contrast between dynamical behavior under different parameters. (a) Chaotic bursting discharge and (b) phase trajectory ($x$–$w$ plane) for $c_3 = 1.05$; (c) periodic spiking discharge and (d) phase trajectory ($x$–$w$ plane) for $c_3 = 1$.

### 3.3. Chaotic robustness

Chaotic robustness refers to the characteristic that chaotic systems can maintain chaotic behavior even when their initial values experience perturbations or disturbances, which means that chaotic systems have a certain degree of anti-interference ability.[44] With parameter values as shown in Table 3 and initial conditions $(x(0), y(0), z(0), w(0)) = (0, y(0), 0.1, 0)$, the bifurcation diagram of the system is obtained, as shown in Fig. 10(a), where the variation range of initial states $y(0)$ is from $-100$ to 100.

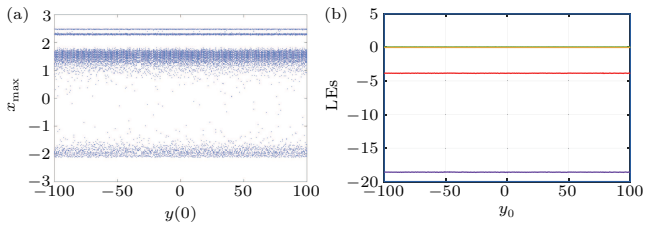



**Fig. 10.** Robustness of chaotic dynamics against initial conditions. (a) Bifurcation diagram and (b) Lyapunov exponents versus initial value $y(0)$ varying from $-100$ to 100.

According to the observation from Fig. 10(a), the system's bifurcation diagram shows a dense set of points with a large-scale range $y(0)$, which indicates that the system does not deviate from the chaotic state due to disturbances of the initial value $y(0)$. Further numerical experiments confirmed that the bifurcation structure of the system remains unchanged under other varying initial conditions, as exemplified in Fig. 10(a). This demonstrates the robustness of its operational mode to initial component variations. Lyapunov exponents in Fig. 10(b) further validate this. In fact, disturbances from other initial components cannot interfere with the chaotic state of the system. Therefore, the system has dynamics similar to neural discharge and chaotic robustness. The FPGA implementation of the proposed system is detailed in the next section.

## 4. FPGA-based hardware implementation

Traditionally, chaotic systems have been predominantly implemented using analog circuits, including experimental boards with discrete components[45–47] and CMOS-based integrated circuits.[48–50] However, these analog implementations are often susceptible to parameter drift caused by environmental factors such as temperature variations, which can compromise control precision. To advance the engineering applications of chaotic systems and enable their efficient control and regulation, a flexible and reconfigurable hardware architecture is essential. The field-programmable gate array (FPGA) platform, renowned for its computational speed, high integration density, and design flexibility, presents an ideal solution for generating precise digital chaotic signals. This section details the FPGA implementation of the proposed chaotic system. The design begins with a numerical solver, and the improved Euler algorithm is adopted as follows:

$$y_{n+1} = y_n + \frac{h}{2}\left[f(x_n, y_n) + f(x_{n+1}, y_n + hf(x_n, y_n))\right]. \quad (10)$$

The discretized system of Eq. (6) is as follows:

$$\begin{cases} x_{n+1} = x_n + \dfrac{h}{2}\left[\left(-a_1x_n^3 + a_2x_n^2 + a_3x_n + a_4z_n - a_5\right) + \left(-a_1x_{\text{pred}}^3 + a_2x_{\text{pred}}^2 + a_3x_{\text{pred}} + a_4z_{\text{pred}} - a_5\right)\right], \\ y_{n+1} = y_n + \dfrac{h}{2}\left[\left(-b_1y_n - b_2\left(z_n + w_n\right)\right) + \left(-b_1y_{\text{pred}} - b_2\left(z_{\text{pred}} + w_{\text{pred}}\right)\right)\right], \\ z_{n+1} = z_n + \dfrac{h}{2}\left[\left(-c_1x_nz_n - c_2x_n^2z_n + c_3y_n\right) + \left(-c_1x_{\text{pred}}z_{\text{pred}} - c_2x_{\text{pred}}^2z_{\text{pred}} + c_3y_{\text{pred}}\right)\right], \\ w_{n+1} = w_n + \dfrac{h}{2}\left(my_n + my_{\text{pred}}\right), \end{cases} \quad (11)$$

where $x_{\text{pred}}$, $y_{\text{pred}}$, $z_{\text{pred}}$, and $w_{\text{pred}}$ represent intermediate values predicted using the Euler method.

The core idea of designing a chaotic signal generator based on FPGA is to divide the entire system into multiple functional modules, including an improved Euler algorithm solving module, a data interception module, a numerical conversion module and a data processing module. The system is implemented on FPGA using the development platform VIVADO 2018.3, and the system parameters are specified in Table 3, with the initial values of $x(0) = 0$, $y(0) = 0$, $z(0) = 0.1$, and $w(0) = 0$. The pin association diagram of FPGA and DAC are given, as shown in Fig. 11. It can be observed from Fig. 11 that there are two input signals and four output signals in total. In the FPGA ACX720, the output signals are digital, while the oscilloscope needs to receive analog signals. Therefore, the signals output by the FPGA need to be converted using a DAC (AN9767) module to generate analog signals. Specifically, four 32-bit digital signals generated by the FPGA correspond to the system's four variables $x$, $y$, $z$ and $w$. They are converted into 14-bit analog signals (o_da_datax, o_da_datay, o_da_dataz, o_da_dataw) to achieve the conversion from digital to analog signals using a digital-to-analog converter DAC (AN9767). Thus, the digital signals generated by the FPGA are output as analog signals displayed on the oscilloscope.

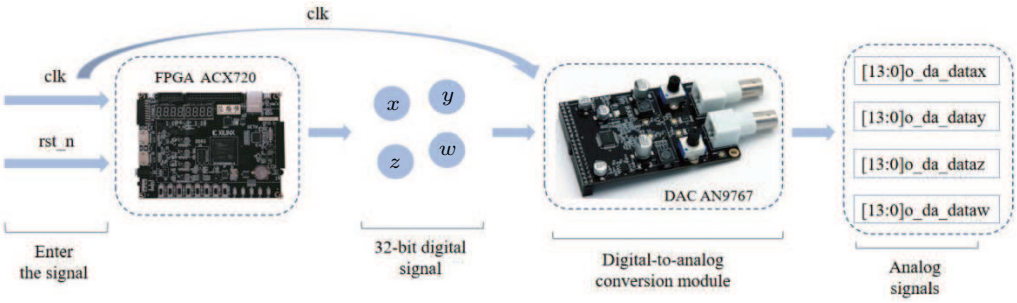
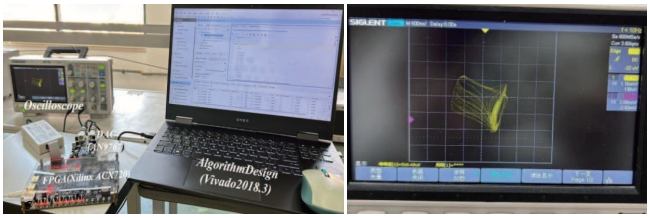



**Fig. 11.** Schematic diagram of FPGA and DAC connection pins.




(a) (b)

**Fig. 12.** Hardware structure and FPGA experimental results. (a) Hardware structure diagram and (b) FPGA-oscilloscope.

The hardware structure of the system and experimental results are given, as shown in Fig. 12. It can be seen from Fig. 12(a) that the experiment requires a VIVADO 2018.3 development platform, an FPGA development board (Xilinx ACX720), a DAC converter (AN9767) and a digital oscilloscope. The FPGA experimental results in Fig. 12(b) completely match the numerical simulations in Fig. 6(b), indicating that the designed FPGA-based memristor chaotic circuit can be implemented.

## 5. Conclusion and perspective

This paper presents a new local active memristor simulator and establishes a memristor-based chaotic circuit system. This system exhibits rich neuron-like discharge dynamics, including periodic spiking, bursting, and chaotic discharge with an alternating spiking and bursting pattern. Mechanism analysis reveals that the spiking-bursting alternating chaotic behavior stems directly from the local activity of the memristor. Furthermore, the system demonstrates strong chaotic robustness across a wide range of parameters. Both FPGA-based hardware experiments and numerical simulations confirm the theoretical findings. Future work will focus on exploring additional dynamical characteristics of this system, aiming to provide foundational support for its application in neuromorphic computing and neural coding.

## Acknowledgments

Project supported by the National Natural Science Foundation of China (Grant No. 62473238), the Shandong Provincial Natural Science Foundation (Grant No. ZR2021MF116), and the Qingdao Natural Science Foundation (Grant No. 23-2-1-233-zyydjch).

## References

[1] Ott E, Spano M and Katz R A 1996 *Phys. Rev. Lett.* **64** 1196
[2] Lorenz E N 1963 *J. Atmos. Sci.* **20** 448
[3] May R M 1976 *Nature* **261** 459
[4] Rössler O E 1976 *Phys. Lett. A* **57** 397
[5] Huang W, Li Y, Huang Y 2021 *Acta Phys. Sin.* **70** 010501 (in Chinese)
[6] Lin H, Wang C, Cui L, Sun Y, Xu C and Yu F 2022 *IEEE Trans. Ind. Inform.* **18** 8839
[7] Lin H, Wang C, Cui L, Sun Y, Zhang X and Yao W 2022 *Nonlinear Dyn.* **110** 841
[8] Yang D, Liu Z and Zhou J 2014 *Commun. Nonlinear Sci. Numer. Simul.* **19** 1229
[9] Wang Z, Min F and Wang E 2016 *AIP. Adv.* **6** 095316
[10] Lin H, Wang C and Tan Y 2020 *Nonlinear Dyn.* **99** 2369
[11] Song Y, Yuan F and Li Y 2019 *Entropy* **21** 678
[12] Yan S, Zhang Y, Ren Y, Sun X, Cui Y and Li L 2023 *Nonlinear Dyn.* **111** 17547
[13] Wang G, Yuan F, Chen G and Zhang Y 2018 *Chaos* **28** 013125
[14] Rajagopal K, Khalaf A J M, Wei Z, Pham V, Alsaedi A and Hayat T 2019 *Int. J. Bifurcat. Chaos* **29** 1950067
[15] Yuan F, Wang G and Wang X 2016 *Chaos* **26** 073107
[16] Ahmadi A, Parthasarathy S, Pal N, Rajagopal K, Jafari S and Tlelo-Cuautle E 2023 *Int. J. Bifurcat. Chaos* **33** 2330016
[17] Li Y, Wang M, Chang H, Wang H and Chen G 2024 *Nonlinear Dyn.* **112** 3851
[18] Bi Q, Zhang R and Zhang Z 2014 *Appl. Math. Comput.* **243** 482
[19] Lin Y, Liu W, Bao H and Shen Q 2020 *Chaos Solitons Fractals* **131** 109524
[20] Chang H, Li Y, Chen G and Yuan F 2020 *Int. J. Bifurcat. Chaos* **30** 2030019
[21] Fallah H 2016 *Int. J. Bifurcat. Chaos* **26** 1630022
[22] Forrest M D 2013 *Plos One* **8** e68765
[23] Bao H, Zhu D, Liu W, Xu Q, Chen M and Bao B 2020 *Int. J. Bifurcat. Chaos* **30** 2050045
[24] Zhao H, Ma X and Bi Q 2024 *Int. J. Non-Linear Mech.* **159** 104592
[25] Chua L 1998 *Int. J. Bifurcat. Chaos* **15** 11
[26] Gibson G A, Musunuru S, Zhang J, Vandenberghe K, Lee J, Hsieh C C, Jackson W, Jeon Y, Henze D, Li Z and Williams R S 2016 *Appl. Phys. Lett.* **108** 023505
[27] Weiher M, Herzig M, Tetzlaff R, Ascoli A, Mikolajick T and Slesazeck S 2019 *IEEE Trans. Circuits Syst. I* **66** 2627
[28] Ascoli A, Slesazeck S, Mähne H, Tetzlaff R and Mikolajick T 2017 *IEEE Trans. Circuits Syst.* **62** 1165
[29] Lai Q, Yang L 2024 *Chaos* **34** 013145
[30] Ying J, Liang Y, Wang G, Iu H, Zhang J and Jin P 2021 *Chaos* **31** 063114
[31] Jin P, Han N, Zhang X, Wang G and Chen L 2023 *Commun. Nonlinear Sci. Numer. Simul.* **117** 106961
[32] Yan X, Li Z and Li C 2024 *Chin. Phys. B* **33** 028705
[33] Wang X, Banerjee S, Cao Y and Mou J 2024 *Chin. Phys. B* **33** 100501
[34] Zhou X, Jiang D, Nkapkop J D D, Ahmad M, Fossi J T, Tsafack N and Wu J 2024 *Chin. Phys. B* **33** 040506
[35] Wang W, Kiss I and Hudson J 2001 *Phys. Rev. Lett.* **86** 4954
[36] Wan Q, Li F, Liu J, Chen S, Yan Z 2023 *Circuits Syst. Signal Process* **42** 623

[37] Xu Q, Wang Y, Wu H, Chen M and Chen B 2024 *Chaos Solitons Fractals* **179** 114458
[38] Boriskov P 2022 *IEEE Trans. Circuits Syst. II Express Briefs.* **69** 2982
[39] Yan S, Song Z and Shi W 2022 *J. Circuits Syst. Comput.* **31** 2250120
[40] Cang S, Wang L, Zhang Y, Wang Z and Chen Z. 2022 *Chaos Solitons Fractals* **158** 112016
[41] Jia H, Chen Z, Shi W and Qi G 2022 *Int. J. Bifurcat. Chaos* **32** 2250022
[42] Gupta M and Chauhan R 2022 *J. Circuits Syst. Comput.* **31** 2250043
[43] Rziga F, Mbarek K, Ghedira S and Besbes K. 2017 *Appl. Phys. A Mater. Sci. Process* **123** 288
[44] Potapov A and Ali M K 2000 *Phys. Lett. A* **277** 310
[45] Zhou L, Wang C and Zhou L 2017 *Int. J. Bifurcat. Chaos* **27** 1750027
[46] Zhou L, Wang C and Zhou L 2018 *Int. J. Circuit Theory Appl.* **46** 84
[47] Zhou L, Wang C and Zhou L 2016 *Nonlinear Dyn.* **85** 2653
[48] Jin J and Li C 2019 *Complexity* **19** 4106398
[49] Zhang X and Wang C 2019 *IEEE Access* **7** 16336
[50] Jin J 2018 *Microelectron. J.* **75** 27